Chapter 3

Structure and Dynamics of the Outer Radiation Belt

Implications for Space Weather Modeling and Forecasting

D. Vassiliadis[1], A.J. Klimas[2], S.F. Fung[2], D.N. Baker[3], R.S. Weigel[3],
S. Kanekal[4]

1. *USRA at NASA/Goddard Space Flight Center, Greenbelt, MD 20771, USA*
2. *NASA/Goddard Space Flight Center, Greenbelt, MD 20771, USA*
3. *LASP, University of Colorado, Boulder, CO 80309, USA*
4. *Catholic University of America, Washington, DC 20007*

Abstract Since the early 1990s a series of spacecraft missions have completely transformed our view of the electron radiation belts. This paper summarizes a number of new results on the structure and dynamics of the belts obtained from those measurements. First, the structure of the outer electron belt is discussed with emphasis on the regions (P_0-P_2) distinguished on the basis of the time variations of the electron flux. Each region is characterized by distinct set of acceleration and loss processes. While these processes are traditionally represented by diffusion models, new empirical models have emerged in the last decade. These models are developed from the observed dynamics of the flux as a function of L shell and energy. We have developed such models in each P_i region, and introduce methods of writing them as empirical diffusion-convection models. Since any realistic space weather model must be driven by interplanetary activity parameters, we discuss the development of input-output models (filters) focusing on those driven by the solar wind velocity. In addition to the plasma velocity, other solar wind and IMF parameters are important for each outer-belt region. Taken together, these parameters describe geoeffective solar wind structures. This precursor information can be used to advance the forecast lead time. The expected impact of these modeling approaches to radiation belt forecasting is discussed.

Keywords Magnetic storms, radiation belts, particle acceleration, MHD waves and instabilities, solar wind, magnetosphere-inner, solar wind/magnetosphere interactions, solar cycle, forecasting, space weather, time series analysis.

I.A. Daglis (ed.), Effects of Space Weather on Technology Infrastructure, 43-64.

1. RADIATION BELT MODELING: FROM SPACE PHYSICS TO SPACE WEATHER

Inner-magnetosphere spacecraft missions of the last decade have highlighted the dynamic and complex nature of the electron radiation belts [Lemaire, 2001]. They have led to new questions regarding the relative efficiency of acceleration and loss processes, and the conditions under which these processes are activated [Li and Temerin, 2001; Friedel et al., 2002]. At the same time the need for space weather forecast products has steadily increased [Baker et al., 2001]. Modern empirical models have been developed to address that need, using the significant knowledge base of mission datasets. The first attempts in real-time prediction at geosynchronous orbit are promising [Baker et al., 1990; Li et al., 2001], while future capabilities and accuracy levels are expected to increase with the advent of data-assimilation techniques [Moorer et al., 1999; Rigler et al., 2004].

Probably more than any other mission, the Combined Release and Radiation Effects Satellite (CRRES) spacecraft demonstrated the dynamic character of the radiation belts. One of the best-studied events has been the March 24, 1991 storm highlighted by the rapid formation of a new radiation belt during storm sudden commencement during the passage of a high-amplitude interplanetary shock [Li et al., 1993]. After its formation deep in the inner magnetosphere at L=2.5, normally a region of relatively low flux due to enhanced precipitation and loss, the belt persisted at least until the mission's end, 6 months from the time of its creation. Following CRRES, the Polar spacecraft [Blake et al., 1995] and Cluster constellation [Daglis et al., 1995] have provided new insights in the composition and energy spectrum of the trapped population.

While unique events, such as the March 1991 storm, reveal novel aspects of the acceleration processes, comprehensive modeling of the radiation belts needs to be based on statistical and comparative studies, and this is the perspective emphasized in the present paper. Statistical and dynamical modeling makes use of the long-term monitoring of the radiation belts by the Solar, Anomalous, and Magnetospheric Particle Explorer (SAMPEX), EXOS-D (Akebono) and its predecessors, the GPS constellation, and the numerous spacecraft at geosynchronous orbit (GEO).

Several of the results reviewed below are based on analysis of data by SAMPEX. This spacecraft is a Small Explorer Mission launched in 1992 into a polar, circular, low Earth orbit (LEO) [Baker et al., 1993]. One might presume that the usefulness of flux measurements by LEO spacecraft like SAMPEX and Akebono may be limited, because they have access only to the off-equatorially-mirroring part of the trapped distribution rather than the full trapped distribution measured by spacecraft at an equatorial orbit, such

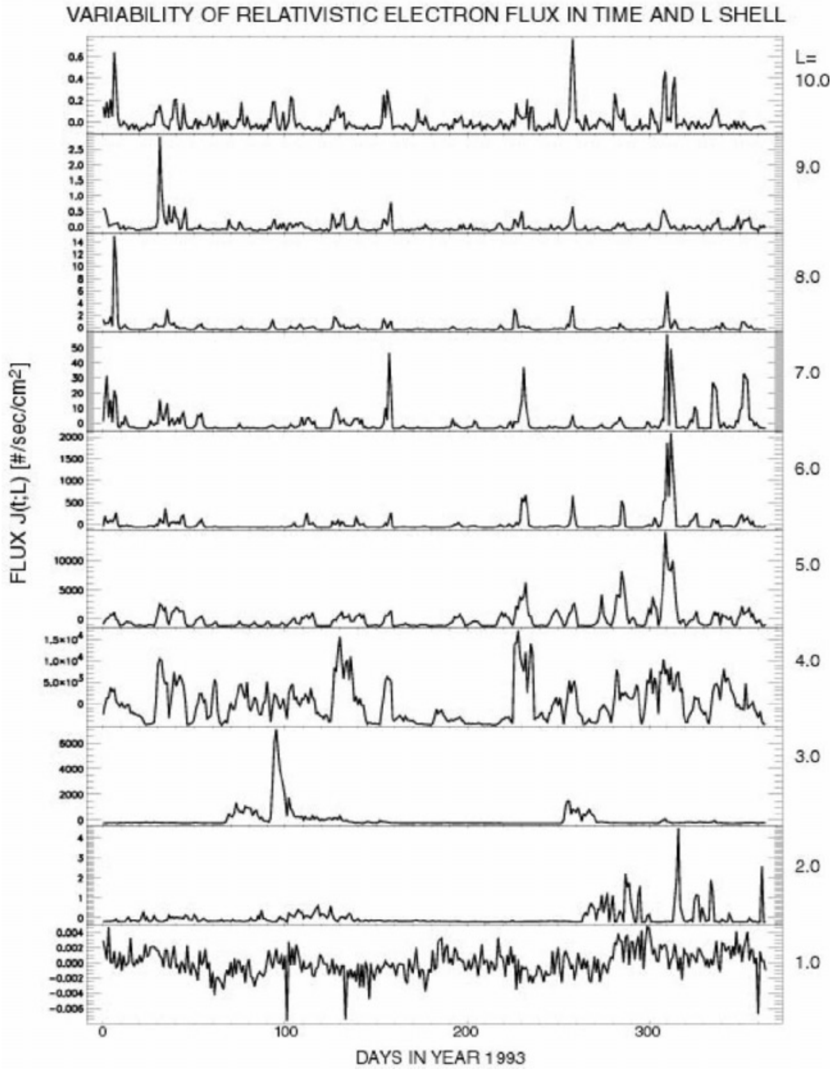

Figure 1. Time and L shell var iability of the omnidirectional relativistic-electron flux j_e(t;L=const.). SAMPEX/PET flux data are shown over the course of one year (1993) and at equidistant L shells.

as CRRES or various GEO spacecraft. Comparison between simultaneous flux measurements, however, has shown that the pitch angle equilibration is rapid, of the order of a few hours, and leads to a coherent response of the inner magnetosphere [Kanekal et al., 2001]. In addition, LEO spacecraft cross a wide range of L shells every few hours, in a traversal, which is fast enough to produce synoptic coverage of the entire radial range of the inner magnetosphere at the timescale of one day. Due to its fast period and solar-cycle-long mission duration, SAMPEX has captured a plethora of radiation-belt phenomena triggered by the passage of various interplanetary structures.

In general both low and high-altitude measurements have demonstrated the extent to which the energetic electron flux varies in a complex manner in both time and space. For instance, Fig. 1 shows the electron flux from SAMPEX's Proton-Electron Telescope (PET) [Cook et al., 1993] at energies of 2-6 MeV. The flux variations are shown at fixed, equidistant L shells ($\Delta L=1.0$) over the course of one year. Note that high-amplitude relativistic electron flux events (electron "storms") may sometimes appear simultaneously over many radial distances, but in general their amplitude and duration differs significantly with altitude. Some storms are observed only in a subset of latitudes and, to complicate things further, measurements at high L shells can sometimes miss signatures of storms entirely while in other regions the instrument may be contaminated or its detectors may be saturated. The spatial and temporal complexity and the small number of simultaneous observational platforms make it difficult to conclusively identify source and loss regions and mechanisms. These difficulties are compounded by the current lack of an accurate magnetic-field model [Selesnick and Blake, 2000].

In the following sections this paper reviews the structure and dynamics obtained from various types of flux data analysis and the prospects of physical and empirical modeling. The following topics are discussed:

- Structure of the outer zone. Section 2 examines the electron flux $J_e(L;E)$ and its correlation as a function of radial distance.
- Flux dynamics resulting from acceleration, loss, and transport. Section 3 is an introduction to the basic processes, and presents the development of empirical models of the flux variations.
- Coupling to interplanetary activity. Geoeffective structures in the solar wind couple to each radial region of the inner magnetosphere in different ways. In Section 4, filter and precursor analysis are used to identify relevant interplanetary inputs and the mechanisms that they drive. At longer timescales, the methods are used to measure the geoeffectiveness of solar wind inputs as a function of solar cycle and season.

2. RADIAL STRUCTURE OF THE RADIATION BELTS

The electron radiation belts constitute a complex plasma system. Its most salient radial feature is the division into the inner and outer belt by the slot region in which electron scattering and loss are maximized. The stationary (time-averaged) radial profile of the flux is well known [Walt et al., 1994] and represented by standard radiation models [e.g., Vette, 1991; Heynderickx, 2002]. A better resolution of the radial structure can be obtained

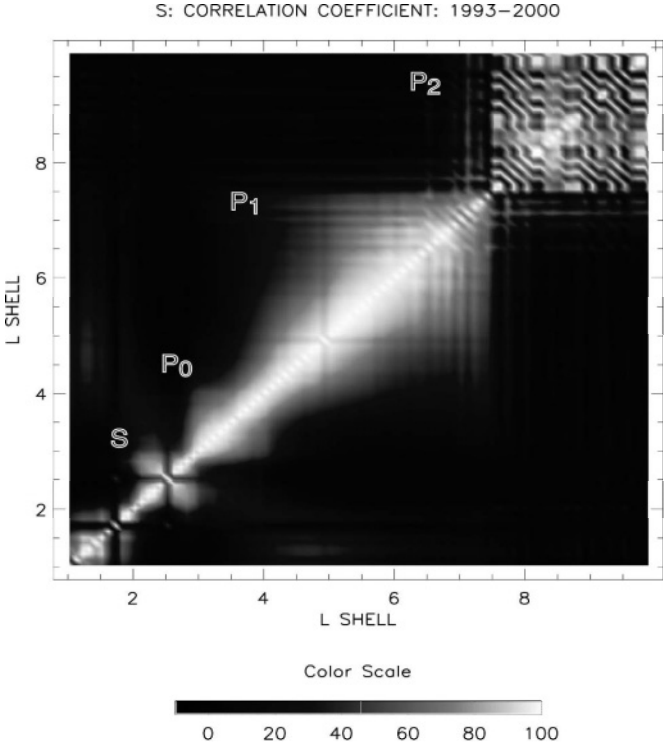

Figure 2. The radial correlation function (1) is calculated from SAMPEX/PET fluxes in the observation interval 1993-2000. Note the division of the outer belt in 3 "blocks," or structures P_0-P_2 of different dynamics. The quadrupole-shaped region below P_0 is the slot (S); the quadrupole shape means that the flux dynamics at the slot edges are strongly correlated with each other suggesting loss processes that operate coherently across the slot.

by examining the flux variation of the radial profile [Vassiliadis et al., 2003b], as will be reviewed below. On the other hand, local time and polar-angle variations of the flux are smaller, because of the high drift velocity and bounce frequency, respectively. Nevertheless, acceleration and loss processes are highly structured in MLT. For instance, the growth of ULF waves, involved in radial diffusion and/or acceleration, is prominent in the dayside and the dawn regions [Anderson et al., 1990; Engebretson et al., 1998].

We discuss the radial structure of the belts in terms of the omnidirectional flux $J_e(t;L;E)$ at shell L and energy E. The time variation of the log-flux at fixed L and E produces the time series j_e(t; L=const.; E=const.). Using low-time-resolution (daily-average) fluxes reduces the significance of individual injections and adiabatic effects. Under those conditions, the time variation of the flux is indicative of the global dynamics of the belts [see also Baker et al.,1999; Kanekal et al., 2001].

To measure the spatial variation of $J_e(t;L)$ we use the radial correlation function:

$$C(L_1,L_2)=\frac{1}{T\sigma_{J_e(L_1)}\sigma_{J_e(L_2)}}\int_{t=0}^{T}\delta J_e(t;L_1)\,\delta J_e(t;L_2)\,dt \qquad (1)$$

where δJ_e is the fluctuation of the flux $J_e(t;L=\mathrm{const})$ from its long-term average, $\sigma_{J_e(L_i)}$ is the standard deviation of the flux distribution in shell L_i; and time T is a long interval of activity (here: years 1993-2000). The L shell range is [1,10] while the energy is fixed at the 2-6 MeV channel of PET. This standard form of correlation takes values in the range [-1,1].

The radial correlation function (1) consists of discrete regions, seen as diagonal blocks in Fig. 2, of high correlation values. Outside these blocks the correlation is low, meaning that the time variations of $J_e(t;L=\mathrm{const})$ varies significantly from one region to another. This view of the outer belt's radial structure stands in direct contrast to the time-averaged profile $J_e(L)$ which varies much more slowly with L than C(L,L).

Region P_1 at L=4.1(±0.2)-7.5(±0.4), is the "heart" of the outer belt, containing by far the largest amount of trapped radiation flux than the other two regions due to its size and flux amplitude. Because L=6.6 falls within that range, the flux variation at the geosynchronous orbit is on average similar to the variation in other L shells, all the way down to L=4. However, solar cycle variations affect the flux at the geosynchronous region much more than the flux at the lower part of region P_1 (see discussion below in this section). Also the geosynchronous orbit is differentiated by other factors from the rest of P_1 such as the response to IMF inputs [Vassiliadis et al., 2004].

Closer to Earth than L=4 is region P_0, at L=3.0(±0.1)-4.0(±0.2) with clearly different dynamics from P_1. The difference between the two regions arises because of different acceleration and loss processes, as well as different types, and degrees, of coupling to the solar wind. The differences are further discussed in Sections 3 and 4, respectively.

At higher L shells than P_1, L>7.5(±0.4), is region P_2 featuring lower-amplitude, transient fluxes. The dynamics of this marginally trapped population is most probably dependent on the plasma sheet penetration into the inner magnetosphere. An alternative view suggests that a significant part of these electrons are accelerated in the cusp [Fritz, 2001; Sheldon et al., 1998]. A third possibility is that the flux dynamics in P_2 is related to the "leakage", or outward transport, of electrons from the main portion of the outer belt [Blake et al., 2002].

Below region P_0, the slot (S) at L=2.0(±0.1)-3.0(±0.1) has a characteristic quadrupolar shape in the correlation function (Fig. 2). This type of shape means that the slot edges are highly correlated and particle loss occurs simultaneously on average. The interpretation is that the causes of loss processes, such as VLF wave fields, vary coherently over a radial range comparable to the slot width.

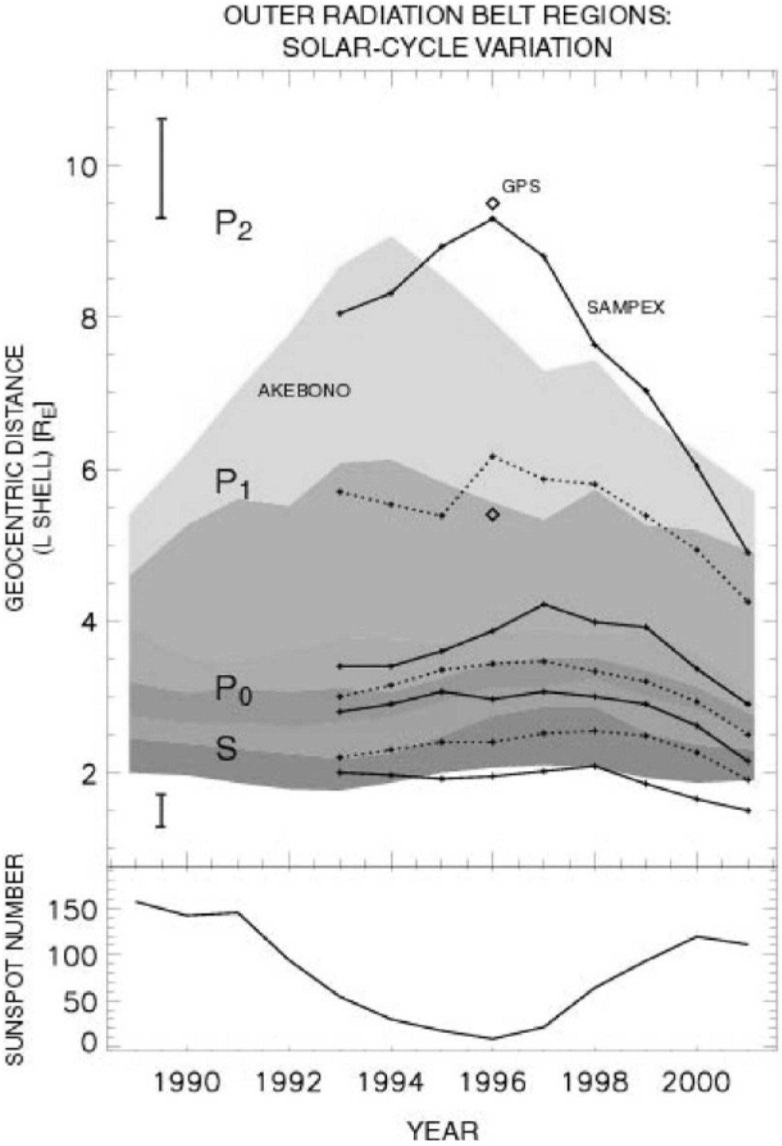

Figure 3. Upper panel: Solar cycle variation of the size of the three regions P_i and the slot. The region boundaries are obtained by Akebono/RDM measurements (regions shown in color; including white for P_2 and black for the slot) and SAMPEX/PET (shown as dotted lines). In 1996, the GPS NS-33 spacecraft provided two measurements for L>4 (shown as diamonds). Within a region, the L shell with the widest correlation length is also indicated (for Akebono: changes in color shading; and for SAMPEX: solid lines). Lower panel: Sunspot number. Note the erosion of P_1 during solar maximum in favor of the quasitrapping region P_2.

Similar results are obtained from three other spacecraft: EXOS-D/Akebono (instrument: RDM), EXOS-C/Ohzora (HEP), and GPS NS-33 (BD II) [Vassiliadis et al., 2003b]. These spacecraft have operated at different altitudes and solar cycle phases, and their instruments have covered different energy ranges.

The time variation of the P_i regions can be followed as a function of solar cycle phase thanks to the long-term observations of Akebono and SAMPEX (Fig. 3). The boundaries and "centers" (points of widest correlation in L) of the three regions are variable with time. The largest radial displacement is that of the P_1-P_2 boundary: during solar maximum, buffeting of the magnetosphere by shocks, CMEs, and other solar wind ejecta reduces the long-trapping region P_1 in favor of the quasi-trapping region P_2. The variability is evidence that the geosynchronous orbit is dominated by different populations and dynamics in the course of the solar cycle. Therefore a realistic model of the geosynchronous region must vary with solar cycle phase.

A similar oscillation can be seen at the boundary between region P_0 (whose greatest radial extent occurs approximately 3 years before solar minimum) and the slot (3 years before solar maximum). In addition to the region boundaries, one can discern a solar-cycle variation in the L shell of the broadest correlation (indicated on Fig. 3).

3. FLUX DYNAMICS DUE TO ACCELERATION AND LOSS PROCESSES

Electron acceleration occurs due to a variety of processes [Friedel et al., 2002]. Important among those are the interaction with low-frequency waves which scatter the electrons in energy and/or pitch angle. Other major processes are direct injection and nonlinear diffusion.

A standard scenario involving ultra-low-frequency (ULF) waves begins with reconnection producing a seed population of electrons (10-100 keV) during storms and substorms. Increases in solar wind velocity V_{SW} excite ultra-low-frequency (ULF) waves in the dayside magnetopause and the flanks [Engebretson et al., 1998; Vennerstrom, 1999] primarily as shear-flow instabilities [Farrugia et al., 2001] and compression. These are consistent with the ULF wave distribution as determined from in situ measurements [Anderson et al., 1990] and remote sensing [e.g., Pilipenko and Engebretson, 2002] (note that there are significant differences between space and ground observations because of ionospheric absorption of the waves). At the end of this growth stage the wave power reaches its peak after 1 day [Rostoker et al., 1998; Mathie and Mann, 2000; O'Brien et al., 2003].

In the second stage the waves accelerate the seed electrons to MeV energies possibly through resonant acceleration. In this type of acceleration there is a resonance

$$\omega - m\omega_d = 0 \tag{2}$$

between the wave frequency ω and the electron drift frequency ω_d. The observational evidence is complemented by numerical experiments in which fields from global MHD simulations are used to drive guiding-center particle codes [Hudson et al., 1999; Elkington et al., 1999, 2003].

Fluxes in the few-MeV range reach their peak after 2-3 days at the geosynchronous region [Paulikas and Blake, 1979; Baker et al., 1990] and more generally in the P_1 region [Vassiliadis et al., 2002]. For a monochromatic wave, the maximum energy gain ΔE_m is the half-width around the resonant frequency ω [Elkington et al., 2003]:

$$\Delta E_m = \sqrt{\frac{2e\delta E_{rm}\delta r}{m\left[\frac{\partial(\ln\omega_d)}{\partial E}\right]_{E=E_m}}}$$

Other factors determining the efficiency of resonant acceleration are the type of resonance (toroidal or poloidal) [Chan et al., 1989; Elkington et al., 1999], the effect of solar wind pressure, etc. Further improvements are expected in the near future since the current global MHD models do not accurately represent the inner magnetosphere structure (e.g., they do not include a ring current), or time dependence (their effective time resolution is typically ~1 min).

In addition to resonant acceleration, other candidate acceleration mechanisms are large- and small-scale recirculation [Nishida et al., 1976], cusp acceleration [Sheldon et al., 1998; Fritz, 2001]; direct injection during substorms [Ingraham et al., 2001]; and enhanced diffusion [Hilmer et al., 2000]. The March 1991 event mentioned in Section 1 highlighted what is probably one of the fastest and most efficient acceleration processes, involving a magnetospheric compression by a high-amplitude interplanetary shock, and the resulting impulsive injection [Li et al., 1993]. ULF-wave-related mechanisms include magnetic pumping via pitch-angle scattering and flux tube motion associated with the waves [Liu et al., 1999]; and cyclotron interaction between trapped electrons and a fast-mode ULF wave [Summers and Ma, 2000]. Finally, loss mechanisms are numerous as well with electron scattering off waves (VLF chorus, whistlers) being two of the most important ones.

While in all these processes, one or more adiabatic invariants are violated resulting in higher fluxes at relativistic energies, adiabatic processes simply displace the particles while preserving the invariants. In the latter case, phase space density is preserved and the electron displacement is temporary. Thus in order to develop a realistic model based on the observed

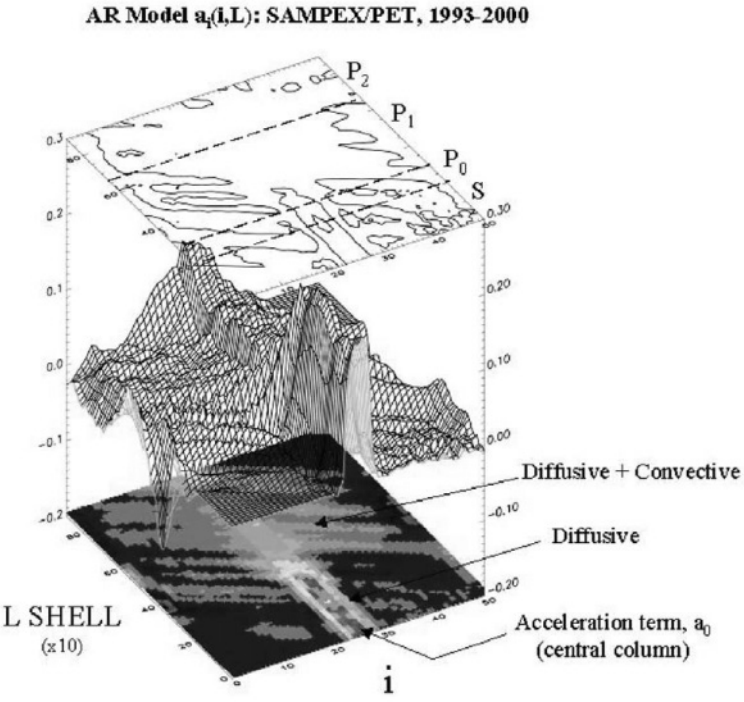

Figure 4a. Radial transport coefficients a_i from AR model (3) as a function of i and L. The left-hand (right-hand) part of the figure indicates transport from lower (higher) L shells, or i<0 (i>0).

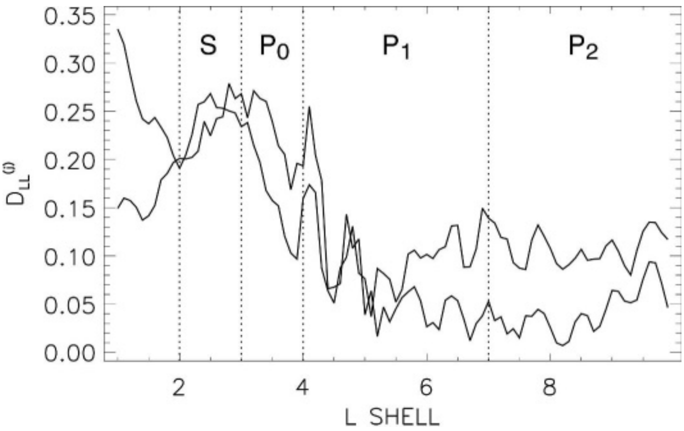

Figure 4b. Diffusion coefficient $D_{LL}^{(j_e)}$ for j_e. Two different ways of calculating it from (5) are shown.

flux variations, the effects of the adiabatic changes need to be removed first. The most important adiabatic effects are the displacement of electrons by an increase in the ring current (the "D_{st} effect") or the tail current. The D_{st} variation accounts only for a small fraction of the storm-time electron flux change [McAdams and Reeves, 2001].

In the following we develop an dynamical empirical model for the time variations of the logarithmic flux (or log-flux) $j_e(t;L;E) = \log_{10} J_e(t;L;E)$ parameterized by L. Adiabatic effects are minimized by the choice of a low time resolution (1 day). We write the log-flux on day t+1 as a function of the log-flux at nearby L shells on day t:

$$j_e(t+1;L) = \sum_{i=-N}^{N} a_i j_e(t;L+i\delta L) \tag{3}$$

where N is a free parameter and δL=0.1 is the resolution in L shell. The 0-th term represents the effect of local acceleration on the flux at fixed L over the course of one day. The terms with $i \neq 0$ indicate transport from lower and higher L shells. The radial range over which $a_i(i)$ is significant determines N, and therefore NδL is a effectively a length scale of spatial correlation (compare Eq. (3) with (1)). This type of model is called autoregressive (AR).

In its current version, the model (3) ignores any effects due to interplanetary input or magnetospheric-activity parameters. These effects are examined in Section 4. In addition, the electron energy is fixed at 2-6 MeV for all L shells. In the next version of the model, energy changes as a function of L will be included.

Solving Eq. (3) for the radial coupling coefficients a_i we find that they are functions of i and L (Fig. 4a). A coefficient at position (i,L) indicates the amplitude of the coupling between $j_e(t;L)$ and $j_e(t;L+i\delta L)$ as follows:

In regions S and P_0 the correlation length is small, N=3. The coefficients $a_i(i)$ are large only close to i=0 and symmetric. Their profile indicates a diffusive process. The effective diffusion coefficient will be discussed below.

On the other hand, regions P_1 and P_2 are characterized by a much larger correlation length (NδL = 2.0-2.2). The coefficients $a_i(i)$ are asymmetric with the parameter i, and are broadly distributed around the central column, i=0. Both these features cannot be explained by diffusion alone and need to include convection as well.

To see the connection between model (3) and diffusive-reactive radial transport consider such a process for j_e:

$$\frac{\partial j_e(t;L)}{\partial t} = \frac{\partial}{\partial L}\left(D_{LL}^{(j_e)} \frac{1}{L^2} \frac{\partial (L^2 j_e)}{\partial L} \right) + V_{conv} \frac{\partial j_e}{\partial L} + S(t;L) \tag{4}$$

where the right-hand side contains a diffusive term with coefficient $D_{LL}^{(j_e)}$. We also include a convective term with speed V_{conv}, and a source term S. A diffusion equation is obtained for the phase space density $f = j_e / p^2$, where p is the relativistic momentum, as an approximation to the Fokker-Planck equation. In that case, however, convective effects are typically neglected [Walt, 1994].

We consider that an injection has just taken place and will not be followed by other injections for some time. In modeling the time decay of the flux we can thus neglect the source term S(t;L). Discretizing (4) in t and L with steps $\delta t=1$ and δL, respectively, assuming that D_{LL} varies slowly with L, we obtain Eq. (3) with

$$
\begin{gathered}
a_0 = 1 + 2\left[\frac{1}{L}\frac{\partial D_{LL}}{\partial L} - D_{LL}\left(\frac{1}{\delta L^2} + \frac{1}{L^2}\right)\right] \simeq 1 - 2D_{LL}\left(\frac{1}{\delta L^2} + \frac{1}{L^2}\right) \\
a_i = \pm\frac{1}{2\delta L}\frac{\partial D_{LL}}{\partial L} + D_{LL}\left(\frac{1}{\delta L^2} \pm \frac{1}{L\delta L}\right) \pm V_{conv}\frac{1}{2\delta L} \simeq D_{LL}\left(\frac{1}{\delta L^2} \pm \frac{1}{L\delta L}\right) \pm V_{conv}\frac{1}{2\delta L} \quad i \gtrless 0
\end{gathered} \tag{5}
$$

A comparison between (5) and (3) yields an effective diffusion coefficient $D_{LL}^{(j_e)}$ for the log-flux (Fig. 4b). Its scaling with L differs significantly from the conventional D_{LL} for the phase space density. Similar scalings are obtained also for the effective convection velocity, V_{conv}.

4. DYNAMIC INPUTS: INTERPLANETARY AND MAGNETOSPHERIC PARAMETERS

Acceleration and loss processes are driven or modulated by changes in the solar wind and the interplanetary magnetic field (IMF). It is therefore important to determine the empirical relations between interplanetary parameters and flux variations. Such empirical relations serve as baseline predictive models driven with time-dependent solar wind inputs [Baker et al., 1990] and can be incorporated in space weather models [Heynderickx, 2002]. In addition to driver inputs, the state of an empirical model can be specified more precisely by additionally using magnetospheric parameters (such as magnetic indices) which provide a specification of the activity level [Fung, 1996].

4.1. Filters

Several interplanetary parameters are important for radiation-belt dynamics. Here we examine the solar wind plasma velocity, V_{SW}. Others are examined elsewhere [Blake et al., 1997; Fung and Tan, 1998; Tsutai et al., 1999; Vassiliadis et al., 2004].

The solar wind velocity is the single most important interplanetary input to the radiation belts. The relative importance of this parameter can be assessed by measuring the higher prediction capability of electron flux dynamics using the V_{SW} input compared to any others. The significance of V_{SW} was determined early on through comparisons between V_{SW} and subsequent relativistic electron fluxes at geosynchronous orbit [e.g., Paulikas and Blake, 1979]. Physically, increases in V_{SW} lead to momentum and energy transfer on the dayside through compressions and at the magnetospheric flanks through shear-flow instabilities such as Kelvin-Helmholtz [e.g., Farrugia et al., 2001]. The effects of the viscous processes are most clearly observed under conditions of a zero or weakly positive IMF B_z. In either scenario, the compression or instability drives ULF waves such as Pc5 (period of 2-10 min) into the magnetosphere [Anderson et al., 1990; Engebretson et al., 1998; Vennerstrom, 1999]. The waves grow significantly ~1 day before the rapid increase of energetic electrons [Rostoker et al., 1998].

The effective coupling between velocity and fluxes is a complex function of L shell. At geosynchronous-orbit altitudes an increase in $V_{SW}(t)$ produces an increase in $j_e(t;L=6.6)$ 2-3 days later [Baker et al., 1990]. Using SAMPEX/PET data we extend the modeling for all L shells in the range L=[1-10] [Vassiliadis et al., 2002]. As a model we use a linear finite-impulse-response (FIR) filter of the form:

$$j_e(t;L_i) = \int_{-T_S}^{T} H(\tau;L_i) V_{SW}(t-\tau)\,d\tau \tag{6}$$

where the log-flux $j_e(t;L) = \log J(t;L)$ as before, the impulse response $H(\tau;L_i)$, parametrized by L_i, is convolved with V_{SW}; the coupling starts at $-T_s$ and ends at time T, both measured in reference to the time of arrival of solar wind at the magnetopause.

The impulse response at geosynchronous-orbit altitude, $H(\tau;L=6.6)$, peaks at $\tau=3$ days (Fig. 5a) in agreement with earlier studies which analyzed geostationary satellite data [e.g., Baker et al., 1990]. The response is calculated from 8 years (1993-2000) of daily averages of V_{SW} and SAMPEX flux measurements so it represents a long-term average [Vassiliadis et al., 2002]. The function becomes negative at $\tau=7$ days meaning that from that time on, variations in V_{SW} are anticorrelated with increases of $j_e(t;6.6)$, or

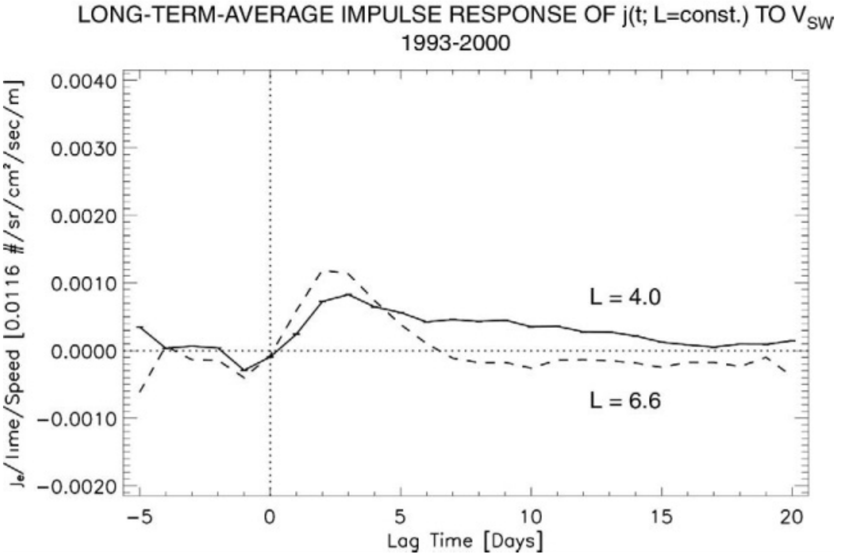

Figure 5a. Impulse response function for V_{SW} from the FIR model (6) for individual L shells, L=4.0 and 6.6. Note the similarity in the location of the $\tau=3$ day peak, subsequent decay, as well as the minimum at $\tau=-1$ day.

particle loss. An earlier minimum at $\tau=-1$ days is due to the adiabatic displacement of electrons by the growth of the ring current. The current intensifies because of enhanced convection caused by a Southward interplanetary magnetic field component. The intensification occurs initially at approximately L=5.5 and then expands radially Earthward and outward.

The second curve in Fig. 5a shows the flux response at L=4.0. The peak position is located close to that of L=6.6; note, however, that $H(\tau;4.0)$ remains positive long after $\tau=7$ indicating stable trapping at this L shell.

Making use of SAMPEX's continuous and broad coverage in L shell, we synthesize a composite impulse response $H(\tau;L)$ from individual response functions calculated at fixed L. The composite function expresses the amplitude and time of the coupling V_{SW}, as well as the radial location where it occurs (Fig. 5b). Peaks P_0 and P_1 correspond to the blocks in the radial correlation graph of Fig. 2. Thus there is a good correspondence between the dependence of long-term flux dynamics on L shell and the flux response to V_{SW} (and other inputs). The correspondence suggests that the dynamics are determined to a great extent by the external forcing rather than by internal processes.

The filters (6) can be interpreted as direct local acceleration due to processes activated by the solar wind speed (such as ULF wave acceleration). Alternatively, increases in $j_e(t;L=\text{const.})$ can be due to transport from higher L shells. The ambiguity between the two inter-

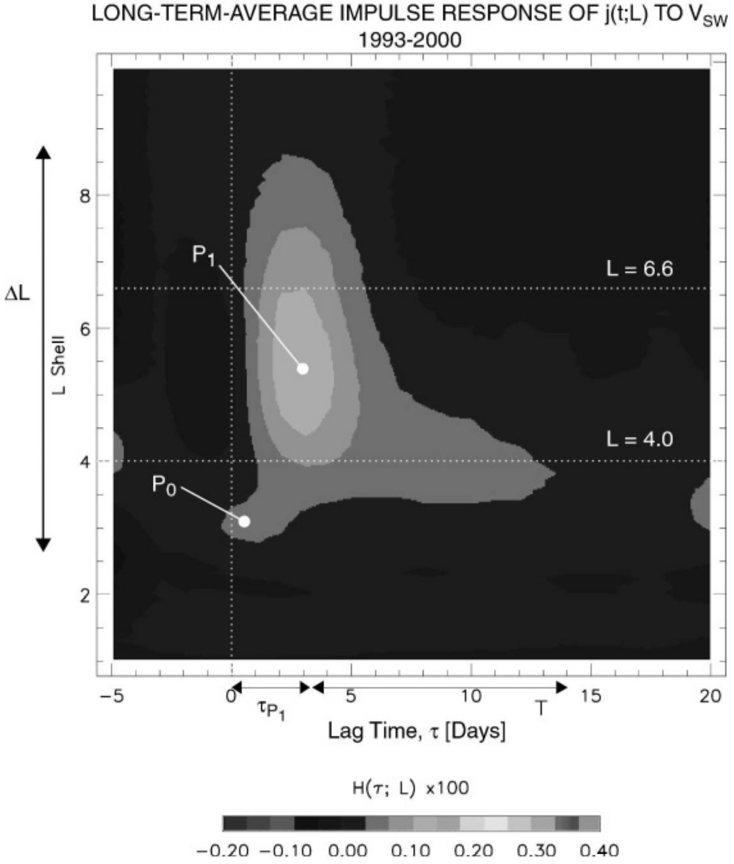

Figure 5b. Impulse responses H(τ;L) for all shells in the L range [1,10]. Note the position and extent of region P_1 (response to high-speed streams) and P_0 (response to CMEs).

pretations arises because the modeling is applied on fluxes at a single energy range, and can be resolved by modeling of flux measurements at multiple energies.

In addition to solar wind velocity, other interplanetary variables are important in controlling the flux dynamics. Earlier studies have shown the significance of the IMF B_z component and density [Blake et al., 1997] as well as magnetospheric indices [e.g., Tsutai et al., 1999]. Vassiliadis et al. [2004] have examined the response of the electron flux in terms of solar or interplanetary variables, or geomagnetic indices which we use as proxies for the regional electrodynamic activity.

We find that a total of 17 such parameters fall into three categories which affect each P_i region in a different way. Hydrodynamic parameters such as V_{SW}, ρ_{SW}, and P_{SW} can predict up to 36% of the variance in P_1 and a smaller amount in P_1. The IMF B_z component, and magnetic indices that

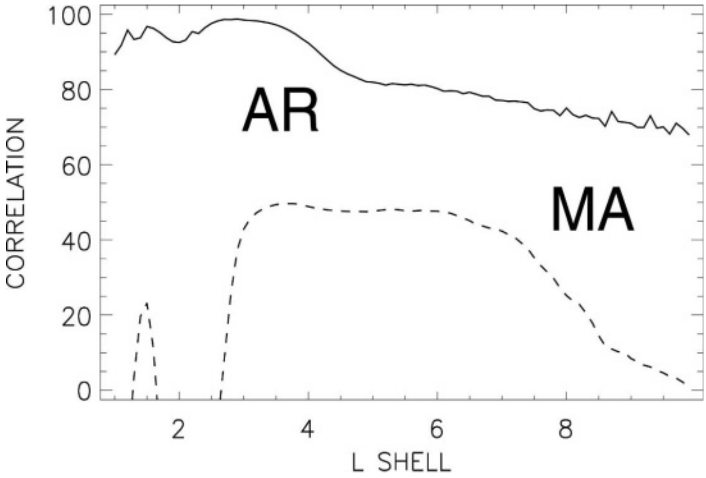

Figure 6. Comparison of the data-model correlations for the AR and FIR (denoted as MA) models. The square of the correlation is the percentage of the variance in the flux data explained by the model.

depend on it, form a second category. The IMF B_z regulates, primarily through the reconnection rate at the magnetopause, the intensity of currents systems such as the ring and tail currents, field-aligned currents, and ionospheric currents. The electrodynamic activity is quantified in terms of regional or planetary measures of geomagnetic activity, which are the geomagnetic indices. Both the IMF B_z and the indices predict the variance of fluxes in P_0 and P_1 in a very similar manner. The indices such as K_p and the polar cap index, PC, are much more accurate, however, predicting the variance of P_1 at a 25% level and the variance of P_0 at a 50% level. Much higher percentages can be explained by AR models such as (3) as Fig. 6 shows. The combination of models (3) and (6) are expected to further increase the explained variance of $j_e(t;L)$.

4.2. Precursors

For an externally driven system like the radiation belts, determining the geoeffective precursor activity is a more direct method than filter analysis for forecasting and modeling. The precursors to an electron acceleration event can be physically interpreted as structures in the solar wind. We briefly sketch out below the precursor analysis which is described at length in [Vassiliadis et al., 2003a]. We denote the daily average $J(t_i;L_j)$ as an event of that amplitude at shell L_j. The precursor to that event, in terms of the solar wind velocity, is the activity vector

$$\mathbf{I}^{(V_{sw})}(t) = [V_{SW}(t-(T-1)),\ldots,V_{SW}(t-(T-1)),V_{SW}(t-T),\ldots,V_{SW}(t+T_s)] \tag{7}$$

or a window in the velocity time series with width $T+T_s$, where generally $T \gg T_s \simeq 0$. Similar precursors can be formed for other solar wind and IMF variables.

Precursors to events of similar activities are averaged together in a superposed-epoch-type analysis. The key is to identify intervals of similar activity over a large and comprehensive dataset. As such a database, we use the SAMPEX/PET daily flux measurements from 1993 to 2000.

The measurements are sorted in order of increasing amplitude and divided in 4 quartiles (indexed by q=1,2,3,4), each comprising ~730 days. The average flux in the q-th quartile is $\left\langle j_e(L) \right\rangle_{(q)}$. The average precursor, $\left\langle \mathbf{I}^{(V_{SW})}(t;L) \right\rangle_{(q)}$, a vector of length $T+T_s$, is obtained by averaging over the corresponding individual precursors (7) for each $j_e(t;L)$ in the q-th quartile. Note that geoeffectiveness is defined as the flux over a given L shell range, and therefore the precursor depends on the choice L shell range.

The most geoeffective precursor is that with the highest q-value (here: q=4) corresponding to the top quartile. It is by construction the average of the solar wind conditions that result in the highest flux at a given L shell, or range. Fig. 7 shows the velocity, IMF B_z (in the GSM coordinate system), and solar wind density V_{SW} for q=4. Precursors are shown for 3 L shell regions: P_1, P_2, and the entire inner magnetosphere (L=1-10). The precursor for P_0 is not different from P_1 at the daily resolution so it is not shown.

First, there is a strong similarity between the precursors of the flux in region P_1 and those of the flux in the entire inner magnetosphere. This is because the total electron flux in P_1 is much higher than for any other region in the outer belt; thus, defining geoeffectiveness for P_1 is generally very similar to defining geoeffectiveness for the outer belt, and even in the entire inner magnetosphere.

Second, the precursors for P_1 and P_2 have opposite orientations in solar wind velocity V_{SW} and density ρ_{SW}. In addition the P_1 precursor has a Southward IMF B_z (middle panel of Fig. 7), consistent with energization through dayside reconnection and, eventually, production of seed electrons. The P_2 precursor is characterized by a Northward IMF B_z., producing a weak reconnection poleward of the cusp. Acceleration in the cusp is well established [Sheldon et al., 1998; Fritz, 2001] and is best observable under Northward B_z conditions. It is also of interest that the most geoeffective precursor for P_2 is a low-speed, high-density structure (top and bottom panels of Fig. 7). In summary, the most geoeffective precursors for P_1 are the least geoeffective for P_2, and vice versa. The contrast between the two regions is discussed in more detail elsewhere [Vassiliadis et al., 2003a].

5. SUMMARY AND DISCUSSION

Input-output analysis of the fluxes in terms of the preceding solar wind/IMF variations shows that geoeffective solar wind inputs are different for each region and at varying degrees: the variance in P_1 flux is partly explained by changes in the solar wind velocity, V_{SW}. The impulse response $H(\tau;L=L_{P1})$ shows a τ=2-3 day delay relative to the arrival of the solar wind. The response occurs for high-speed streams and is particularly well-known for $j_e(L=6.6)$. The impulse response in P_0 peaks more rapidly, at $\tau<1$ day, a response which is consistent with recent observations during magnetic cloud and interplanetary CME passages. A different set of precursors is found for the third region, P_2. Thus the input-output analysis suggests that, as the turbulent interplanetary input varies randomly, it excites the three regions as nonlinear modes of the inner magnetosphere.

Synoptic flux measurements over the entire radial extent of the radiation belts allow us to model the temporal dynamics of the flux and determine the corresponding spatial structure in unprecedented ways. Correlation analysis has revealed three regions of distinct dynamical behavior, identified in regions P_0 (L=3-4), P_1 (L=6-7.5), and P_2 (L>7.5). Flux dynamics in the slot S (L=2.0-3.0) are different from any of the three regions. The dynamics itself as obtained from AR modeling can be classified as diffusion- or convection-like. The functional form in regions S and P_0 is consistent with diffusion while regions P_1 and P_2 include additional convection terms in their equations.

In practical terms, a first notable point is that the differences between regions P_i should be taken into account in regional modeling. A model which is accurate in reproducing fluxes at L=6.6 will be significantly than a model at lower L shells in P_1 or P_2. Second, a combination of the FIR and AR models (Eq. (6) and (3)) is expected to result in more sophisticated models with better prediction capabilities for $j_e(t;L)$.

More generally, dynamic modeling is expected to contribute to our understanding and lead to improvement in the predictive capabilities of radiation environment models. These models are used in tandem with radiation effects models to quantify the space weather hazards on specific spacecraft components. Current models have evolved from the static NASA AE-8 model [Vette, 1991], but are still limited in spatial and temporal coverage [Heynderickx, 2002]. This is the main reason due to which the traditional models are still the industry standard. Integrated approaches such as the interaction between empirical and physical models promoted by the Center of Integrated Space Weather Modeling (CISM) are expected to further improve the predictability of the radiation belt environment.

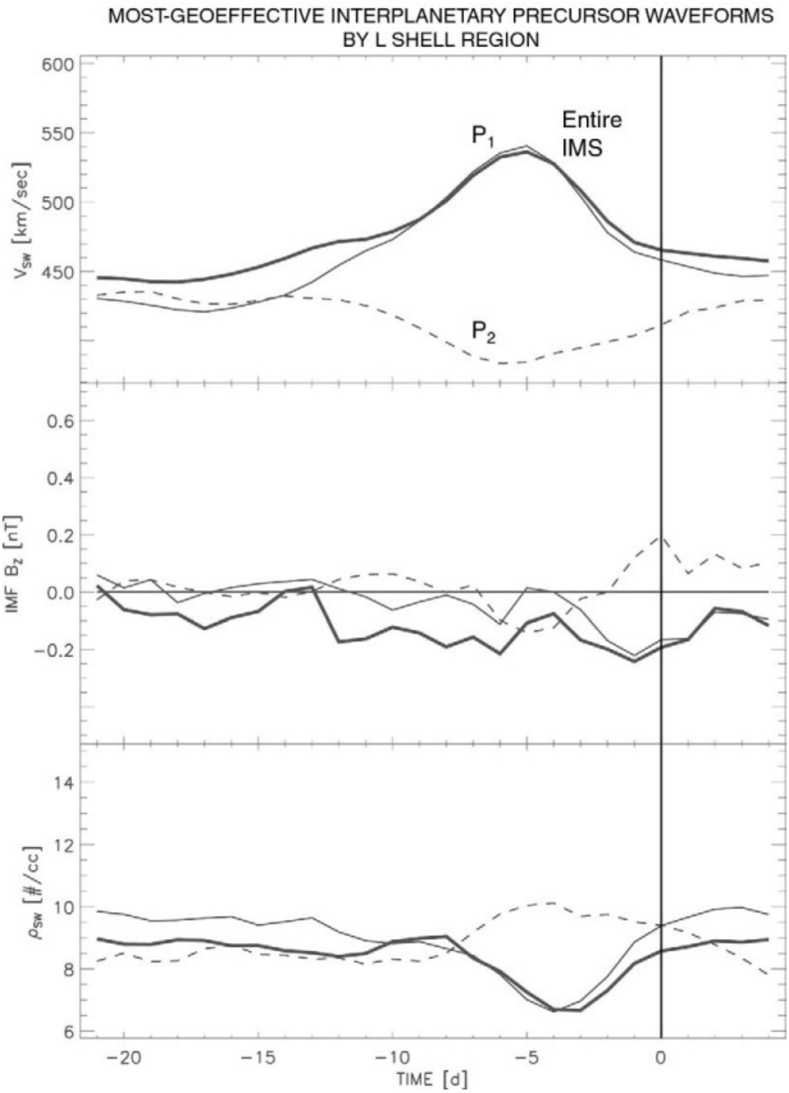

Figure 7. Precursors for P_1, P_2, and the entire inner magnetosphere (L=[1-10]). Precursors are shown in terms of V_{SW}, IMF B_z, and ρ_{SW} for the last T=20 days before a high-amplitude event (also shown are the T_s=5 days following the event).

6. ACKNOWLEDGMENTS

We are thankful to the ESPRIT organizers, and especially Ioannis Daglis, for the invitation to present this review to the Advanced Research Workshop. We thank J. Fennell for discussions, and the referee for a number of comments and suggestions. T. Nagai and R. Friedel provided flux measurements from several spacecraft. Research was supported by the NASA/LWS TR&T program and the NASA/NSSDC research program. We also thank the data providers in NSSDC, and the Kyoto and Copenhagen World Data Centers.

7. REFERENCES

Anderson, B.J., M.J. Engebretson, and S.P. Rounds, A statistical study of Pc 3-5 pulsations observed by the AMPTE/CCE magnetic fields experiment 1. Occurrence distributions, J. Geophys. Res. 95, A7, 10,495-10,523, 1990.

Baker, D. N., R. L. McPherron, T. E. Cayton, R. W. Klebesadel, Linear prediction filter analysis of relativistic electron properties at 6.6 RE, J. Geophys. Res. 95, A9, 15,133-15,140, 1990.

Baker, D.N., G.M. Mason, O. Figueroa, G. Colon, J.G. Watzin, R.M. Aleman, An overview of the Solar, Anomalous, and Magnetospheric Particle Explorer (SAMPEX) mission, IEEE Trans. Geosci. Rem. Sens., 31, 3, 531-541, 1993.

Baker, D.N., S.G. Kanekal, A.J. Klimas, D. Vassiliadis, T.I. Pulkkinen, Collective phenomena in the inner magnetosphere, Phys. Plasmas 6, 11, 4195-4199, 1999.

Baker, D.N., Satellite anomalies due to space storms, in: *Space Storms and Space Weather Hazards*, I.A. Daglis (ed.), pp. 285-311, NATO Science series, Kluwer Academic Publishers, Dordrecht, 2001.

Blake, J.B., J.F. Fennell, L.M. Friesen, B.M. Johnson, W.A. Kolasinski, D.J. Mabry, J.V. Osborn, S.H. Penzin, E.R. Schnauss, H.E. Spence, D.N. Baker, R. Belian, T.A. Fritz, W. Ford, B. Laubscher, R. Stiglich, R.A. Baraze, M.F. Hilsenrath, W.L. Imhof, J.R. Kilner, J. Mobilia, D.H. Voss, A. Korth, M. Gull, K. Fisher, M. Grande, and D. Hall, CEPPAD, in: Russell, C.T., (ed.), *The Global Geospace Mission*, Kluwer Academic, Dordrecht, the Netherlands, 1995.

Blake, J.B., D.N. Baker, N.Turner, K.W. Ogilvie, R.P. Lepping, Correlation of changes in the outer-zone relativistic-electron population with upstream solar wind and magnetic field measurements, Geophys. Rev. Lett. 24, 8, 927-929, 1997.

Blake, J.B., J.L. Roeder, R.J. Selesnick, D.N. Baker, P. Daly, M. Grande, M. Carter, Cluster-Polar simultaneous observations of energetic particles in the plasma sheet – evidence for radiation belt leakage?, Eos Trans. AGU 83 (47), Fall Meet. Suppl. SM51A-0502, 2002.

Chan, A.A., L. Chen, and R.B. White, Nonlinear interaction of energetic ring current protons with magnetospheric hydromagnetic waves, Geophys. Res. Lett. 16, 1133-1136, 1989.

Cook, W.R., A.C. Cummings, J.R. Cummings, T.L. Garrard, B. Kecman, R.A. Mewaldt, R.S. Selesnick, E.C. Stone, D.N. Baker, T.T. Von Rosenvinge, J.B. Blake, L.B. Callis, PET- A Proton Electron Telescope for studies of magnetospheric, solar, and galactic particles, IEEE Tras. Geosc. Rem. Sens. 31, 3, 565-571, 1993.

Daglis, I.A., B. Wilken, and E.T. Sarris, *Proceedings of the Cluster-RAPID Science Workshop*, *MPAE-W-056-95-01*, Max-Planck-Institut für Aeronomie, Katlenburg-Lindau, Germany, 1995.

Elkington, S.R., M.K. Hudson, A.A. Chan, Acceleration of relativistic electrons via drift-resonant interaction with toroidal-mode Pc5 ULF oscillations, Geophys. Res. Lett. 26, 21, 3273-3276, 1999.

Elkington, S.R., M.K. Hudson, and A.A. Chan, Resonant acceleration and diffusion of outer zone electrons in an asymmetric geomagnetic field, J. Geophys. Res. 108, A3, 1116, doi: 10.1029/2001JA009202, 2003.

Engebretson, M., K.-H. Glassmeier, M. Stellmacher, W.J. Hughes, H. Luehr, The dependence of high-latitude Pc5 wave power on solar wind velocity and on the phase of high-speed solar wind streams, J. Geophys. Res. 103, A11, 26,271-26,283, 1998.

Farrugia, C.J., F.T. Gratton, R.B. Torbert, Viscous-type processes in the solar wind-magnetosphere interaction, Space Sci. Rev. 95, 1-2, 443-456, 2001.

Friedel, R.H.W., G.D. Reeves, T. Obara, Relativistic electron dynamics in the inner magnetosphere – a review, J. Atmos, Sol.-Terr. Phys. 64, 2, 265-282, 2002.

Fritz, T.A., The cusp as a source of magnetospheric energetic particles, currents, and electric fields: a new paradigm, Space Sci. Rev. 95, 469-488, 2001.

Fung, S.F., Recent developments in the NASA trapped radiation models, in: *Radiation Belts: Models and Standards*, J.F. Lemaire, D. Heynderickx, and D.N. Baker (eds.), Geophysical Monograph 97, American Geophysical Union, Washington, DC, 1996.

Fung, S.F., and L.C. Tan, Time correlation of low-altitude relativistic trapped electron fluxes with solar wind speeds, Geophys. Res. Lett. 25, 13, 2361-2364, 1998.

Heynderickx, D., Radiation belt mod elling in the framework of space weather effects and forecasting, J. Atm. Sol.-Terr. Phys. 64, 1687-1700, 2002.

Hilmer, R.V., G.P. Ginet, T.E. Cayton, Enhancement of equatorial energetic electron fluxes near L=4.2 as a result of high-speed solar wind streams, J. Geophys. Res. 105, 23311-23322, 2000.

Hudson, M.K., S.R. Elkington, J.G. Lyon, C.C. Goodrich, T.J. Rosenberg, Simulation of radiation belt dynamics driven by solar wind variations, in: *Sun-Earth Plasma Connections*, J.L. Burch, R.L. Carovillano, and S.K. Antiochos (eds.), Geophysical Monograph 109, American Geophysical Union, Washington, DC, 1999.

Ingraham, J.C., T.E. Clayton, R.D. Belian, R.H.W. Friedel, M.M. Meier, G.D. Reeves, and M.G. Tuszewski, Substorm injection of relativistic electrons to geosynchronous orbit during the great magnetic storm of March 24, 1991, J. Geophys. Res. 106, 25,759-25,776, 2001.

Kanekal S.D., D.N. Baker, J.B. Blake, Multisatellite measurements of relativistic electrons: global coherence, J. Geophys. Res. 106, A12, 29,721-29,732, 2001.

Lemaire, J.F., From the discovery of radiation belts to space weather perspectives, in: *Space Storms and Space Weather Hazards*, I.A. Daglis (ed.), NATO Science Series, 79-102, 2001.

Li, X., I. Roth, M. Temerin, J.R. Wygant, M.K. Hudson, and J.B. Blake, Simulation of the prompt energization and transport of radiation belt particles during the Marth 24, 1991 SSC, Geophys. Res. Lett. 30, 22, 2423-2426, 1993.

Li, X., and M.A. Temerin, The electron radiation belt, Space Sci. Rev. 95, 1-2, 569-580, 2001.

Li, X., M. Temerin, D.N. Baker, G.D. Reeves, D. Larson, Quantitative prediction of radiation belt electrons at geostationary orbit based on solar wind measurements, Geophys. Res. Lett. 28, 9, 1887-1890, 2001.

Liu, W.W., G. Rostoker, and D. N. Baker, Internal acceleration of relativistic electrons by large-amplitude ULF pulsations, J. Geophys. Res. 104, A8, 17,391-17,407, 1999.

Mathie, R.A., and I.R. Mann, A correlation between extended intervals of ULF wave power and storm-time geosynchronous relativistic electron flux enhancements, Geophys. Res. Lett. 27, 3261-3264, 2000.

Moorer, D.F., D.N. Baker, and S.F. Fung, Estimating outer radiation belt electron flux by data assimilation (unpublished), 1999.

McAdams, K.L., and G.D. Reeves, Non-adiabatic response of relativistic radiation belt electrons to GEM magnetic storms, Geophys. Res. Lett. 28, 1879-1882, 2001.

Nishida, A., Outward diffusion of energetic particles from the Jovian radiation belt, J. Geophys. Res. 81, 1771-1773, 1976.

O'Brien, T.P. K.R. Lorentzen, I.R. Mann, N.P. Meredith, J.B. Blake, J.F. Fennell, M.D. Looper, D.K. Milling, and R.R. Anderson, Energization of relativistic electrons in the presence of ULF power and MeV microbursts: evidence for dual ULF and VLF acceleration, J. Geophys. Res. 108, A8, Art. No. 1329, 2003.

Paulikas, G.A., and J.B. Blake, Effects of the solar wind on magnetospheric dynamics: energetic electrons at the sunchronous orbit, in: *Quantitative Modeling of Magnetospheric Processes*, W.P. Olson (ed.), Geophysical Monograph 21, American Geophysical Union, Washington, DC, 1979.

Pilipenko, V.A., and M.J. Engebretson, Ground images at high-latitudes of ULF wave processes in the outer magnetosphere, J. Atmos. Sol.-Terr. Phys. 64, 2, 183-201, 2002.

Rigler, E.J., D.N. Baker, R. Weigel, D. Vassiliadis, A. Klimas, Adaptive Linear Prediction of Radiation Belt Electrons Using the Kalman Filter, Space Weather (in print), 2004.

Rostoker, G., S. Skone, and D.N. Baker, On the origin of relativistic electrons in the magnetosphere, Geophys. Res. Lett. 25, 3701-3704, 1998.

Selesnick, R.S., and J.B. Blake, On the source location of the radiation belt relativistic electrons, J. Geophys. Res. 105, A2, 2607-2624, 2000.

Sheldon, R.B., H.E. Spence, J.D. Sullivan, T.A. Fritz, J. Chen, The discovery of trapped energetic electrons in the outer cusp, Geophys. Res. Lett. 25, 1825-1828, 1998.

Summers, D., and C.-Y. Ma, Rapid acceleration of electrons in the magnetosphere by fast-mode MHD waves, J. Geophys. Res. 105, 15,887, 2000.

Tsutai, A., C. Mitsui, T. Nagai, Predictions of a geosynchronous electron environment with in situ magnetic field measurements, Earth, Plan. Space 51, 3, 219-233, 1999.

Vassiliadis, D., A. J. Klimas, S. G. Kanekal, D. N. Baker, R. S. Weigel, Long-term average, solar-cycle, and seasonal response of magnetospheric energetic electrons to the solar wind speed, *J. Geophys. Res.*, 10.1029/2001JA000506, 2002.

Vassiliadis, D., R.S. Weigel, A.J. Klimas, S.G. Kanekal, R.A. Mewaldt, Modes of energy transfer between the solar wind and the inner magnetosphere, Phys. Plasmas 10 (2), 463-473, 2003a.

Vassiliadis, D., A.J. Klimas, R. S. Weigel, D. N. Baker, E. J. Rigler, S. G. Kanekal, T. Nagai, S. F. Fung, R. W. H. Friedel, and T. E. Cayton, Structure of Earth's outer radiation belt inferred from long-term electron flux dynamics, Geophys. Res. Lett., 30(19), 2015, doi:10.1029/2003GL017328, 2003b.

Vassiliadis, D., S.F. Fung, and A.J. Klimas, Interplanetary and magnetospheric state parameters for radiation belt electron flux models, submitted, 2004.

Vennerstrom, S., Dayside magnetic ULF power at high latitudes: A possible long-term proxy for the solar wind velocity?, J. Geophys. Res. 104, A5, 10,145-10,157, 1999.

Vette, J.I., The AE-8 trapped electron model environment, NSSDC WDC-A-R&S, 91-24, 1991.

Walt, M., *Introduction to Geomagnetically Trapped Radiation*, Cambridge University Press, Cambridge, UK, 1994.